



PAPER

Robust selective weighted field mapping using multi-echo gradient echo-based MRI

RECEIVED
24 May 2018REVISED
4 September 2018ACCEPTED FOR PUBLICATION
1 October 2018PUBLISHED
23 October 2018Chemseddine Fatnassi¹ and Habib Zaidi^{1,2,3,4,5} ¹ Division of Nuclear Medicine and Molecular Imaging, Geneva University Hospital, CH-1211 Geneva, Switzerland² Geneva University Neurocenter, University of Geneva, CH-1205, Geneva, Switzerland³ Department of Nuclear Medicine and Molecular Imaging, University of Groningen, 9700 RB, Groningen, Netherlands⁴ Department of Nuclear Medicine, University of Southern Denmark, DK-500, Odense, Denmark⁵ Author to whom any correspondence should be addressed.E-mail: habib.zaidi@hcuge.chKeywords: MRI, field map, GRE, quantitative T_2^* map, phase unwrapping**Abstract**

In 3D gradient echo (GRE) and echo planar imaging (EPI), strong macroscopic field gradients are observed at air/tissue interfaces. The respective field gradients lead to an apparent increase in intravoxel dephasing, and, subsequently, to signal loss or image distortion. We propose an analytical approximation and a consequent method to compute low and high resolution field maps over all field map regimes (small and large echo spacing). A number of approaches which compute field maps from reconstructed phase data rely upon optimized linear least square fit and complex division approaches owing to the simplicity of their implementation. Most of these techniques, however, have historically considered only the phase signal when computing off-resonance maps while ignoring magnitude data. This latter may be of notable interest since the presence of noise is well depicted and interpreted. The presence of noise and phase aliasing that increase with increasing echo time (TE) and echo spacing (Δ TE) may seriously challenge the off-resonance map accuracy. These techniques still remain subject to the trade-off during the choice of GRE sequences, TE and Δ TE. In this work, we explore a novel model that considers any type of TE and Δ TE regime (small or large) and high phase wraps complexity. The field offset is weighted by the magnitude signal decay quality, to make the field mapping procedure as noise independent as possible. The performance of the proposed method was tested using simulated, experimental phantoms and *in vivo* human studies. The proposed approach markedly outperforms conventional techniques. It provides a correction equivalent to that of the conventional techniques in regions with high SNR (≥ 20), yielding a mean error of about 0.1 Hz, but appearing more robust in regions with low SNR (≤ 10), such as near the sinus cavity and at the very edge of the brain (mean error less than 1 Hz), where phase wraps and noise are highly present. The proposed technique shows promise to enhance field map generation over any acquisition regime and in regions of both high and low SNR and it can be easily implemented for rapid computation and used in a clinical setting.

1. Introduction

Quantitative magnetic resonance imaging (MRI) is becoming an increasingly useful tool in a number of clinical and research applications of this imaging modality. Unlike transmission and emission imaging modalities (e.g. CT, PET, SPECT...), MRI is a phase-sensitive imaging modality. Both phase and magnitude data are acquired after MR raw data reconstruction. Very useful information encoded into the phase could be derived, which is of crucial importance in several applications if used to yield information about macroscopic static field inhomogeneity (Bernstein *et al* 2004).

Measuring the spatial variation of the macroscopic field (B_0 field mapping) is essential for automatic shimming. It is also necessary for many image reconstruction methods that attempt to correct from B_0 inhomoge-

neity-induced geometric distortions and signal loss (Jezzard 1995, Reber 1998, Yablonskiy 1998, Seara 2000, Dahnke and Schaeffter 2005, Hernando 2010, Yang 2010, Yablonskiy *et al* 2013, Fatnassi *et al* 2017). Moreover, it is also used in phase contrast angiography and other emerging applications, such as MR temperature mapping and MR elastography (Bernstein *et al* 2004). It has been applied for blood oxygenation level dependent (BOLD) contrast studies (Gati *et al* 1997, Zwaag *et al* 2009) and to assess brain iron concentration (Haacke *et al* 2005), dynamic susceptibility contrast MRI (Grandin 2003, Wirestam 2010) and cerebral venous blood volume measurement (An and Lin 2003).

A set of compromises is taken into account to achieve accurate field map generation when multi-echo acquisition is used. A large echo spacing (ΔTE) and echo train length (TEs) may account for undesired phase wraps and image quality degradation (low SNR). The phase data may be overwhelmed by unwanted artefacts and become more arduous to interpret. To overcome the resulting inaccuracies, various post-processing solutions for phase unwrapping have been proposed (Costantini 2002, Cusack and Papadakis 2002, Robinson 2014, Fatnassi *et al* 2015b), based on either spatial (Dagher *et al* 2014) or temporal (Robinson *et al* 2014) unwrapping.

Field mapping regimes are defined by the choice of ΔTE . We can identify three types, the first of which is Regime I, where ΔTE is large enough to allow complex phase wraps occurrence. In Regime II, ΔTE is small enough that noise appears as the dominant artefact. Regime III would use a moderate ΔTE . More detailed descriptions are available in Dagher *et al* (2014).

Reber *et al* (1998) computed the field map from ten acquired echoes (over regime III). Phase data are unwrapped along the temporal dimension and the field map is calculated by scaling the slope of the linear fit. A Gaussian filter is also applied to minimize noise effects. Later, Windischberger *et al* (2004) generated a field map (over regimes II–III) using a linear regression over three echoes corrected from wraps followed by median and Gaussian filtering. Indeed, the mentioned techniques lean on a large number of echoes to provide an accurate field map, but do not consider the noise effect on signal evolution as a function of time. Additional filtering may affect spatial resolution of the measurements.

In 2007, a three-point field mapping was introduced in Aksit *et al* (2007) (over regimes II). To enhance robustness to noise and remove phase unwrapping from the last phase data, the acquired phase images are used in pairs. The wraps were estimated from the two first echoes and removed from the last one. Beyond the time saved by using only a few echoes, noise is still not considered and errors still exist near phase discontinuities and regions suffering from large field inhomogeneities. Funai *et al* (2010) proposed regularized field map estimation (over regimes I–II) that integrates a regularized least-squares cost function in the regression model. The method significantly improves the quality of field map estimates relative to conventional techniques but still relies on regression, which is very time consuming and operates under the assumption that field maps are generally smooth functions, which may not be the case in the presence of large macroscopic field inhomogeneities. More recently, a novel three-echoes field map estimation method (over regimes I–III) was introduced (Dagher *et al* 2014). This approach requires additional echo time (TE) optimization to yield low SNR field map acquisition. Therefore, additional acquisition is needed to acquire offset maps. Furthermore, the method was limited by the extreme low SNR (worst case SNR = 10).

To the best of our knowledge, none of the existing models deal with long echo train length acquisition (long TEs), where echo series are acquired at long TE and under all regime constraints (small and large ΔTE , low SNR and high phase wraps) that concurrently consider magnitude signal decay quality to further optimize field map accuracy and perform a fast computation. This reflects the temporal signal behaviour in the presence of moderate or severe inhomogeneous magnetic field that may result in fast and noisy signal decay across echo times due to low SNR and large susceptibility difference artefacts.

In this work, we propose a new analytical approach for high and low resolution field mapping that is not subject to ΔTE choices. The field map is computed from the complex data using a selective phase unwrapping and a modified four-quadrant tangent function. Phase offset-map computation is weighted by the magnitude signal decay quality to limit noisy echoes contribution. No prior knowledge about optimal TE, ΔTE , SNR or additional acquisition parameters are required, and the computation time is drastically reduced, thus enabling its use in clinical routine. In the following section, we provide a brief theoretical description of the proposed model.

2. Theory

The MR signal in a 3D gradient echo sequence for a given n th voxel acquired in the presence of inhomogeneous magnetic field ΔB_n that is assumed to be equivalent through all vector position directions \vec{r} can be written as:

$$S_n(k; TE_N) = \int_{-\infty}^{+\infty} \rho_n(\vec{r}, TE_N) \exp(-2i\pi k \cdot \vec{r}) d\vec{r} \quad (1)$$

where ρ_n is the ideal signal decay in the absence of field inhomogeneities, N is the echo number and TE is the echo time. The integral limits may change with the slice profile shape that we approximate when performing a Fourier transform. The k -space is conventionally defined as:

$$2\pi k_x = \gamma G_x t_x \quad 2\pi k_y = \gamma G_y t_y \quad 2\pi k_z = \gamma G_z t_z \quad (2)$$

where G_x and G_y are the phases encoding and G_z the readout, $t(x, y, z)$ is the duration of the gradients and γ is the gyromagnetic ratio. After applying the inverse Fourier transform (IFT), we produce independent complex images that contain magnitude and phase information. We consider a particular pixel and denote its complex value in the first and N th image as:

$$\begin{aligned} \chi_{1,n,r} &= x_{1,n} + iy_{1,n} = \rho_{1,n,r} e^{i\varphi_{1,n,r}} \\ &\vdots \\ \chi_{N,n,r} &= x_{N,n} + iy_{N,n} = \rho_{N,n,r} e^{i\varphi_{N,n,r}} \end{aligned} \quad (3)$$

where N is the echo number and n denotes the pixel coordinates. Here, ρ and φ represent complex signal magnitude and phase, respectively. In this work, we aim to estimate the field map by exploiting jointly all phase data at different echo times and the corresponding magnitude signal decay quality. We propose an efficient and quick approach to performing an analytical approximation of the phase difference instead of a numerical regression.

2.1. Selective phase unwrapping

The effectiveness of phase unwrapping techniques frequently relies upon the accuracy of the initial phase assessment, thereby demanding additional adjustment of sequence parameters. It should be noted that phase unwrapping algorithms are computationally time consuming, particularly in two-dimensions (2D) and higher where the unwrapping complexity becomes harder (Dagher *et al* 2014). In MGRE sequences, temporal unwrapping may be of enormous efficiency in real time phase unwrapping over the fourth dimension. Nevertheless, this is only feasible if the initial phase is acquired without any wraps, which is achievable in cases of short TE and small Δ TE acquisition. Those parameters may be chosen to be as small as necessary. Ideally, they should be set to $\pi/(\gamma|\Delta B_{\max}|)$ (Robinson *et al* 2014).

To overcome temporal phase unwrapping failure, especially when a large Δ TE is used (regime I), we introduce a novel algorithm that combines temporal unwrapping with a 2D selective phase unwrapping. In the following explanation of the unwrapping steps, we consider the worst scenario of MGRE acquisition with a large echo spacing (Δ TE = 2.5 ms).

- Step1:** Phase data series are unwrapped over the fourth dimension using a temporal phase unwrapping described previously in Robinson *et al* (2014). Matlab (Math Works Inc., Natick, MA) has an ‘unwrap’ function, which implements a numerical algorithm for phase unwrapping;
- Step2:** Phase difference map is computed using the modified four-quadrant arctangent function detailed in the next subsection;
- Step3:** Differential map is computed from the resulting phase difference map. We should emphasize that we calculate differences between adjacent elements (voxels) and not a gradient map that relies on central difference approximation for field gradient estimation;
- Step4:** Residual wraps from the first temporal unwrapping are identified on the differential map for pixels with a value higher than $|\pi|$;
- Step5:** Only slices containing corrupted pixels are chosen for an additional spatial unwrapping. For that, we used the 2D algorithm devised by Ghiglia and Romero (Ghiglia and Romero (1994) that uses weighted (or unweighted) least-square phase unwrapping.

2.2. Modified four-quadrant arctangent function for phase difference extraction

The phase difference map is computed from the unwrapped phase data using a modified four-quadrant arctangent function that combines the basic atan2 function (Bernstein *et al* 2004) with magnitude signal decay weighting factor reported in equation (6). The function takes two input arguments: imaginary and real part of the first and N th echoes ($\chi_{1,n,r} \dots \chi_{N,n,r}^*$), with ‘*’ denoting the complex conjugate. All phase differences are estimated between the first and subsequent echoes, not between successive echoes. Thereafter, phase signal for each voxel is weighted by the corresponding magnitude signal decay quality. Assuming that magnitude and phase signals vary only slightly within the pixels; the spatial dependency is removed using the following approximations:

$$\begin{cases} \rho_{j,n}(r) \rightarrow \langle \rho_j(r) \rangle_n \rightarrow \rho_{j,n} \\ \varphi_{j,n}(r) \rightarrow \langle \varphi_j(r) \rangle_n \rightarrow \varphi_{j,n} \end{cases} \quad (4)$$

If ΔTE is set to be equal to TE (e.g. low resolution and regimes II–III data presented in this work: $TE/\Delta TE = 1.23/1.23$ ms), we substitute TE_N by $N \cdot \Delta TE$. Otherwise, we keep TE_N (e.g. high resolution and regime I data: $TE/\Delta TE = 2.2/2.5$ ms). To further simplify the expression, pixel coordinates have been dropped for clarity and the field map ΔB is computed for one image pixel as follows:

$$\Delta B = \frac{1}{\gamma \pi N \Delta TE} \cdot \begin{cases} \arctan \sum_{j=1}^N \frac{\Im[\chi_1 \chi_j] \psi_j}{[\Im[\chi_1 \chi_j]^2 + \Re[\chi_1 \chi_j]^2]^{1/2} + \Re[\chi_1 \chi_j]} & \text{for } \Re[\chi_1 \chi_j] > 0 \\ \arctan \sum_{j=1}^N \frac{[[\Im[\chi_1 \chi_j]^2 + \Re[\chi_1 \chi_j]^2]^{1/2} - \Re[\chi_1 \chi_j]] \psi_j}{\Im[\chi_1 \chi_j]} & \text{for } \Re[\chi_1 \chi_j] < 0, \Im[\chi_1 \chi_j] \neq 0 \\ \frac{\pi}{2} & \text{for } \Re[\chi_1 \chi_j] > 0, \Im[\chi_1 \chi_j] = 0 \\ -\frac{\pi}{2} & \text{for } \Re[\chi_1 \chi_j] < 0, \Im[\chi_1 \chi_j] = 0 \\ 0 & \text{for } \Re[\chi_1 \chi_j] = 0, \Im[\chi_1 \chi_j] = 0 \end{cases} \quad (5)$$

where $\chi_1 \chi_j = \rho_1 \rho_j e^{i\Delta\varphi_j}$, \Re and \Im denote real and imaginary parts of the complex data, respectively, and γ is the gyromagnetic ratio, while ψ_j describes the signal decay quality weighting factor and is calculated as follows:

$$\psi_j = \frac{|\rho_j|}{\sum_{j=1}^N |\rho_j|} \cdot \frac{\sum_{j=1}^N \sigma_j}{\sigma_j} \quad (6)$$

where σ_j denotes the signal noise computed as the local standard deviation. Since the field map values are weighted by ψ_j , the field estimation is more dependent on the early echoes, which have better SNR. One can notice that the solution concerning a null imaginary part in equation (5) ranges from $|\pi/2|$ to zero. Nonetheless, this may result in an undefined solution if another four-quadrant function is used. To this end, it is highly recommended to check the specific results that the function may return under specific conditions which may vary among different implementations (Bernstein *et al* 2004).

3. Materials and methods

Three methods for generating field maps using two or all image data are described below. The proposed algorithm is referred to as selective weighted field mapping (SWFM). In the second method, referred to as linear least square fit (LLSf), all images acquired at different echo times are used. The temporal phase signal was unwrapped using conventional temporal unwrapping. The slope of the phase as a function of echo time was determined from LLSf. The field map was generated by scaling this slope. Complex-division (CD) would generate properly reconstructed field maps from only the first two acquisitions. As this approach assumes a small ΔTE between the first two echoes to prevent phase wrapping, no additional phase unwrapping is performed beforehand. The field magnitude difference is computed as:

$$\Delta B = \frac{1}{\gamma 2\pi \Delta TE} \angle(\rho_1 \rho_2 e^{i\Delta\varphi}) \quad (7)$$

where \angle denotes the angle operator.

3.1. Numerical phantom study

To test our hypothesis and proposed algorithm, we developed a numerical phantom using customized Matlab scripts (Math Works Inc., Natick, MA). The phantom contains concentric tubes with an internal and external radius of 12 and 40 mm, filled with air and water. The field distribution and magnetic susceptibility are analytically known ($\chi_{\text{air}}/\chi_{\text{water}} = 3.06 \times 10^{-7}/9.35 \times 10^{-6}$ SI). The inner tube was filled with air, whereas the space between the tubes was filled with water. The magnitude signal of the MGRE sequence was generated using an analytical solution of the Bloch equation:

$$S_n(TE_N) = \frac{M_{n,0} \exp\left(\frac{-TE_N}{T_2^*}\right) \sin(\alpha) \left(1 - \exp\left(\frac{-TR}{T_1}\right)\right)}{1 - \cos(\alpha) \exp\left(\frac{-TR}{T_1}\right)} \quad (8)$$

where $M_{n,0}$ is the ideal signal free from the field gradient inhomogeneities and α is the flip angle. Relaxation times T_2^* and T_1 were set to mimic our *in vivo* values ($T_2^*/T_1 = 60/500$ ms). To evaluate signal noise and phase wrap effects in more detail and over a wider range than under the experimental condition, a total of 40 echoes were simulated using the following sequence parameters: $TR/TE_1/\Delta TE = 47/1.23/1.23$ ms, flip angle 10° , matrix

size of 128×128 and 1 mm^2 in-plane resolution. Phase data were simulated by taking typical phase values from an *in vivo* experiment on a 3T MRI scanner. A typical offset of ± 2 Hz was introduced to create a linear phase shift. To evaluate the effect of noise that might corrupt field map generation accuracy, we corrupted the complex data by adding independent and identically distributed Gaussian noise depending on the simulated SNR magnitude as follows:

$$\varepsilon_{\text{phase}} = \frac{1}{\text{SNR}_{\text{Magnitude}}} \quad (9)$$

where $\varepsilon_{\text{phase}}$ denotes the introduced phase noise. Equation (9) indicates that voxels with high SNR produce low errors in the phase measurement (Fatnassi *et al* 2017). The noisy image was obtained using the following equation:

$$I_{\text{Noisy}} = I + \text{Rand}(I) \cdot \sigma^{1/2} \quad (10)$$

where *Rand* denotes a random variable generator, *I* and I_{Noisy} denote original and corrupted images, respectively, and σ is the noise standard deviation calculated as follows:

$$\sigma = 10^{(0.1 \cdot \text{SNR})} \cdot \text{VAR}(I) \quad (11)$$

where SNR is the desired output image SNR and VAR is the variance operator.

The simulated model enables comparison of all methods for generating field maps using a reference one. This approach also enables the evaluation of standard methods and their robustness in the presence of noise and phase nonlinearity. The analytical solution of the field distribution that we use as reference field map is simulated via different orientations of the phantom with respect to the main static field B_0 . For more detailed descriptions, we refer interested readers to Aksit *et al* (2007). The field map was generated from phase and magnitude images using the three mentioned methods and compared to the analytical field distribution. To control the strength of each strategy for field map generation, we computed the root mean square error (RMSE) for each of the single orientations described above. For qualitative evaluation, the performance of all three approaches was assessed for high and low SNR cases.

A detailed evaluation of the proposed selective phase unwrapping is beyond the scope of this paper. However, the performance of the proposed technique was briefly assessed in this work. Different spatial phase wrap complexities were generated on simulated 3D multi-echo phase data. The original phase consists of a single 3D Gaussian distribution with the maximum value centred in the centre of the matrix. The matrix size was $32 \times 32 \times 32$ and 1 mm^3 of spatial resolution. The complex topographies were introduced using a phase wrap operator available as Matlab function. Phase evolution with time was simulated using different ΔTEs to achieve the different complexity levels ($\text{TE}_1/\Delta\text{TE}_1/\Delta\text{TE}_2/\Delta\text{TE}_3/\Delta\text{TE}_4 = 1/2/3/5/8$ ms), and a typical phase offset equal to the original phase values were used to create ΔB phase behaviour dependent. A total of ten echoes were generated for each echo spacing scenario, and performance of the selective phase unwrapping was compared to temporal, 2D and 3D spatial unwrapping algorithms described in Costantini (2002), Cusack and Papadakis (2002), respectively.

3.2. Experimental phantom and *in vivo* studies

To verify our simulation algorithm, we built a physical phantom comprising concentric tubes filled with air and water mimicking the numerical phantom. The analytical field distribution was compared to the measured one. *In vivo* human data were also acquired to assess the performance of the different algorithms on generating field maps from real data. All scans were performed on a 3T Magnetom Trio (Siemens Healthcare, Erlangen, Germany) using 32-channel phased array coil. The MGRE acquisition parameters are presented in table 1.

4. Results

4.1. Simulation study

Figure 1 depicts the phantom together with plots of the field distribution profile along the *x*-axis, demonstrating a similar field pattern between simulations and experimental results with a small shift caused by the distorted cylindrical phantom used for measurements. The maximum and minimum field variations were measured as 4 Hz and -10 Hz, respectively, which corresponds to the simulated values within an error of 10%.

Figure 2 shows the selective phase unwrapping algorithm pipeline. The phase images are unwrapped using a temporal unwrapping over the temporal dimension, after which phase difference maps are reconstructed. One can observe that residual phase wraps still exist, especially at the very edge of the brain (arrows). Differential maps are calculated, and voxels that contain wraps are identified. Subsequently, only image slices with phase aliasing are spatially unwrapped.

Table 1. Multi-echo gradient echo acquisition parameters. TE/ Δ TE/TR/FA denote echo time, echo spacing, repetition time and flip angle, respectively.

		Acquisition parameters						Number of echoes
	Mode	TE ₁ (ms)	Δ TE(ms)	TR(ms)	Matrix size	Voxel size	FA(°)	
Acquisition1	Low resolution regime II–III	1.23	1.23	47	136 × 136 × 112	1.6 mm ³	8	32 bipolar GRE
Acquisition2	High resolution regime I	2.2	2.5	23.7	240 × 256 × 176	1 mm ³	6	8 FLASH GRE

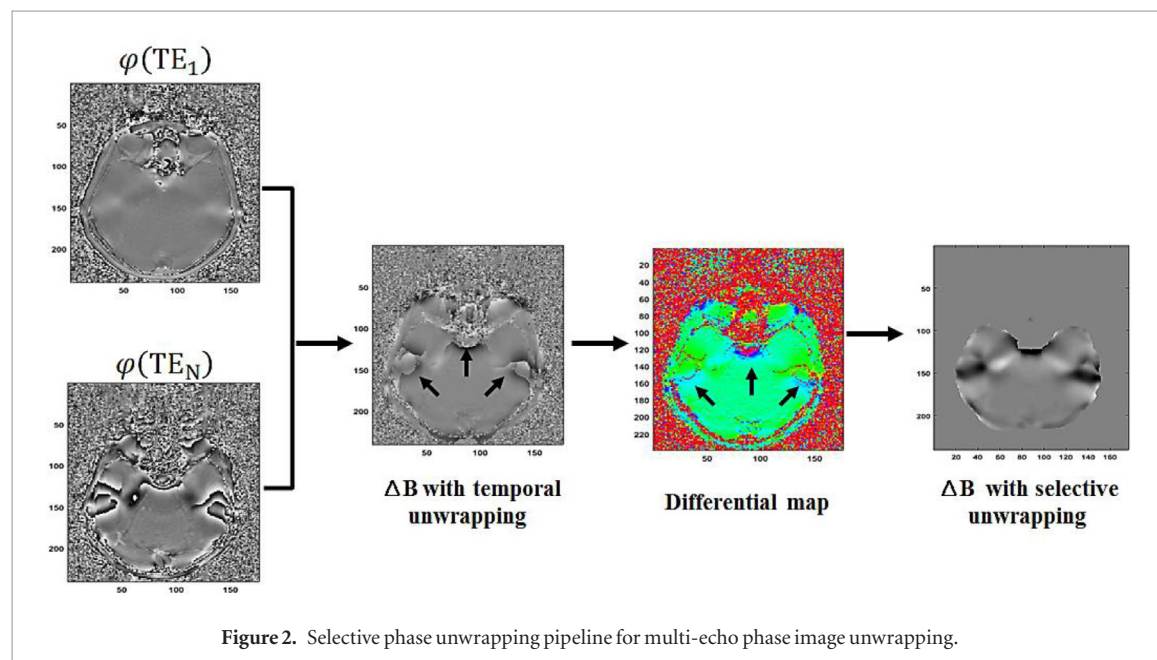
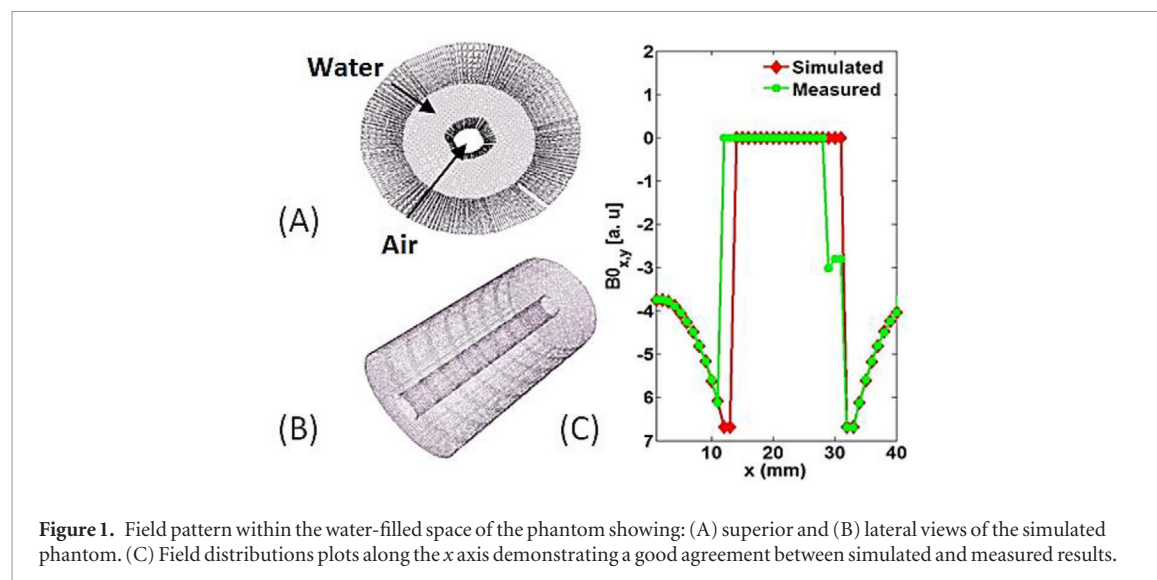


Figure 3 demonstrates representative results achieved by selective phase unwrapping, temporal, 2D and 3D spatial algorithms in unwrapping complex topographies. The last simulated phase echoes, which correspond to the achieved complexity levels for each Δ TE, are shown in two different planes (xy and yz) to better illustrate the spatial phase wraps distribution. The selective phase unwrapping simultaneously provides both unwrapped single phase and phase difference maps, which allows for comparison with spatial unwrapping algorithms. One can notice that increasing spatial wraps complexities may limit most of the techniques. 2D phase unwrapping begins to generate errors at level 2. Beyond, the technique fails totally in unwrapping the complex wraps. Both temporal and 3D unwrapping make errors at unwrapping difficulty levels 3 and 4, but succeed in unwrapping difficulty

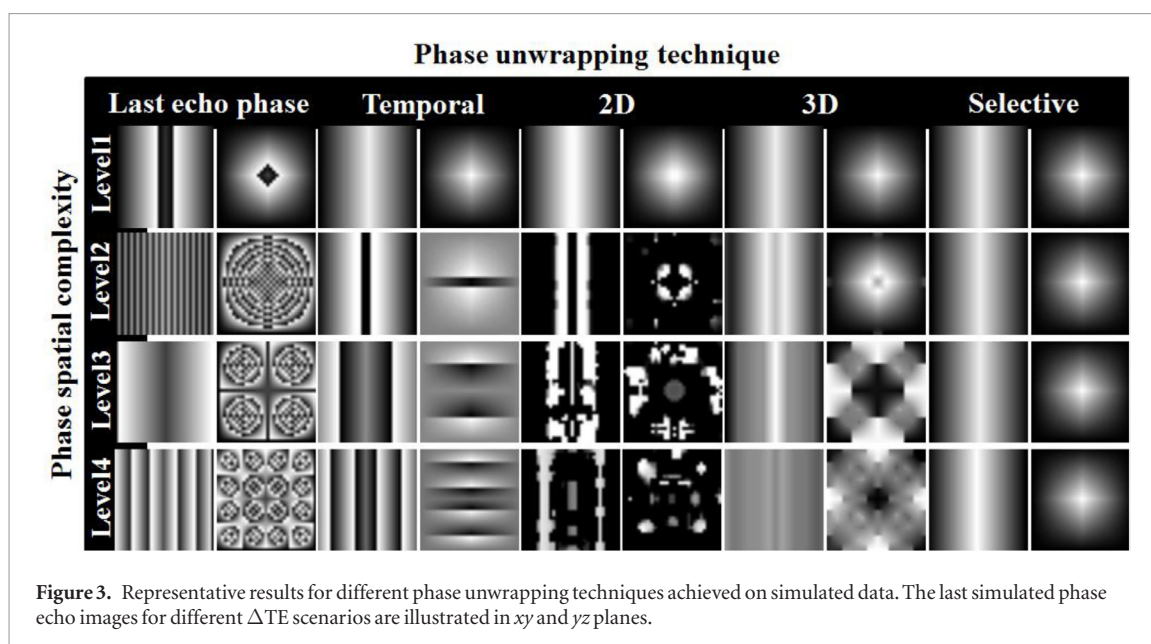


Figure 3. Representative results for different phase unwrapping techniques achieved on simulated data. The last simulated phase echo images for different ΔTE scenarios are illustrated in xy and yz planes.

levels 1 and 2. Selective phase unwrapping makes no unwrapping errors at any difficulty level. The approach was also shown to be much faster than the spatial unwrapping techniques.

Figure 4 illustrates the residual error maps for evaluating the accuracy of the three algorithms in generating field maps as a function of different levels of SNR for $\theta = 90$ and $\Phi = 0$, where θ and Φ are the rotation angles about x and y axes, respectively. In the presence of high SNR (>25), all methods provide accurate field maps compared to the analytical field distribution at different rotation angles (θ , Φ) with respect to the main static field B_0 . SWFM and LLSf demonstrated the best performance in estimating the field map with the least possible errors. The complex division method results in small errors in estimating offsets near the air/water interfaces. For SNR = 25, CD shows a slight inaccuracy and the field map appears noisy. However, both SWFM and LLSf are by far more robust in generating accurate offset maps. In the presence of low SNR (≤ 5), the complex division approach presents the worst results. As expected, the proposed approach performs in a similar way to LLSf even in the presence of a high noise level.

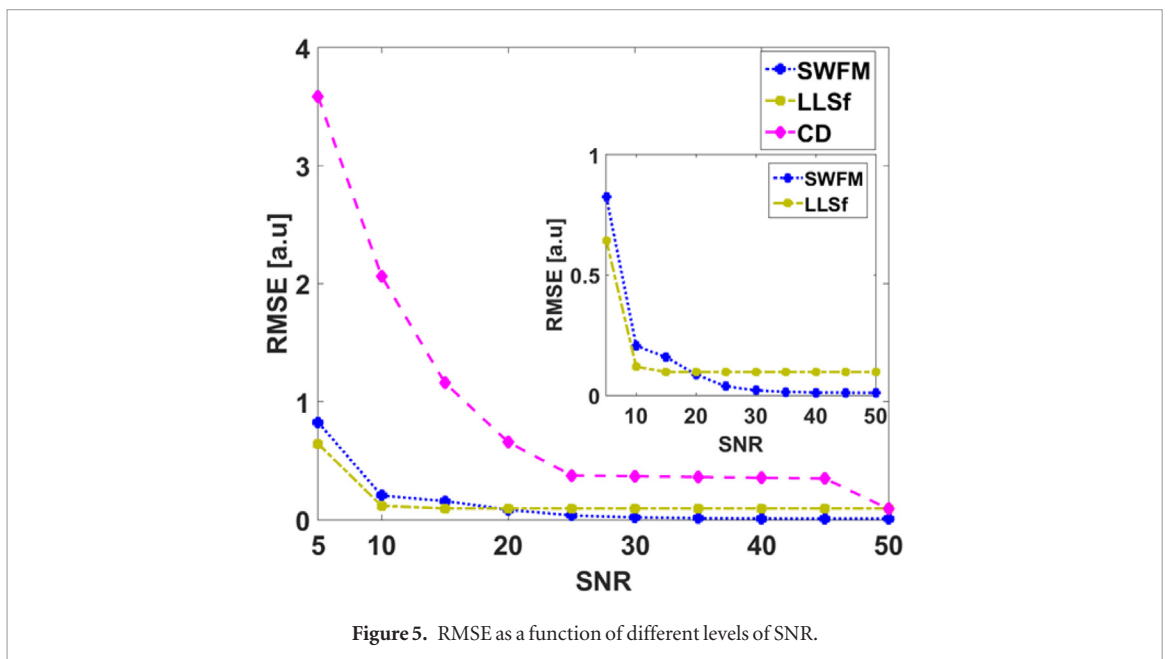
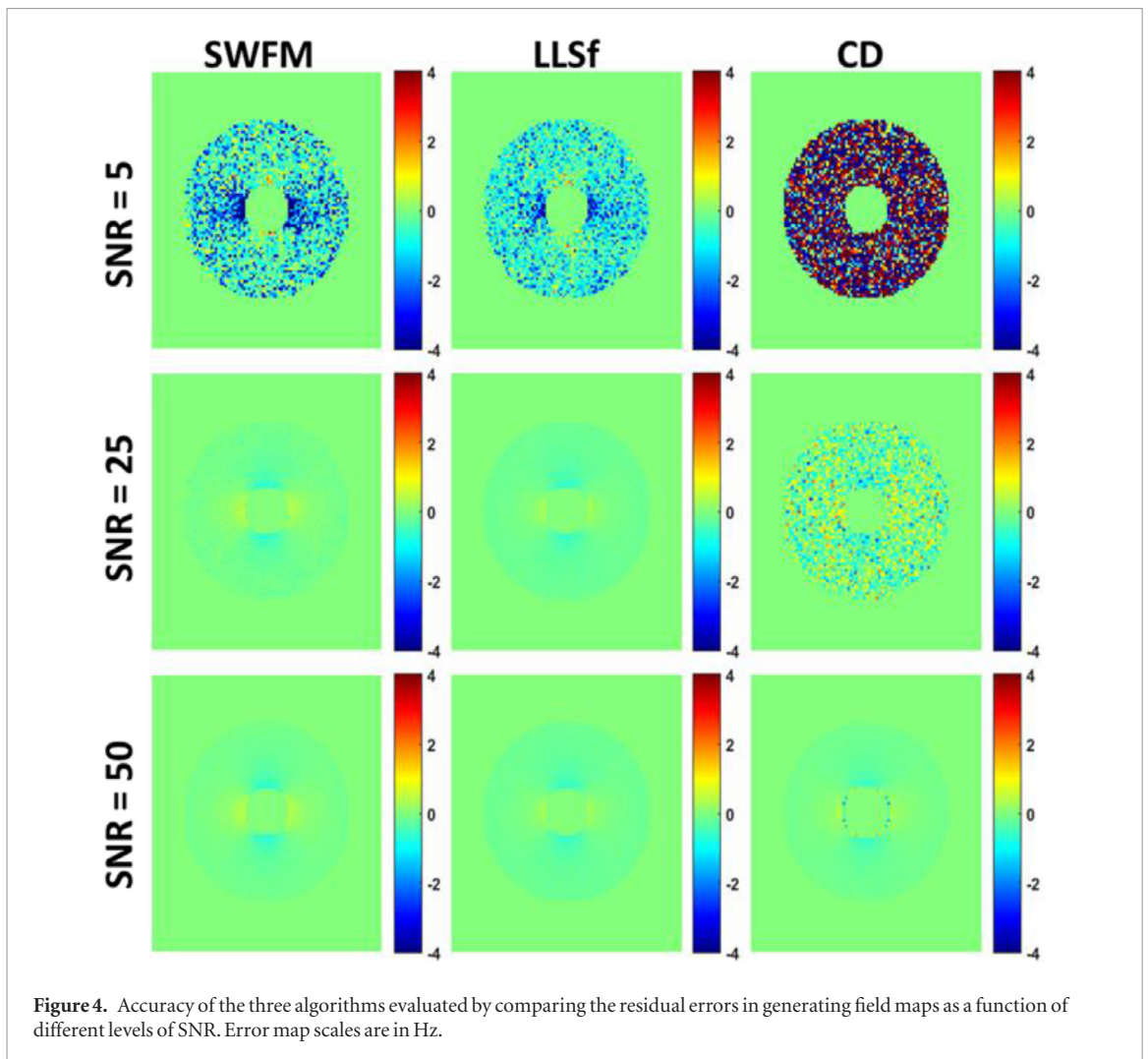
The measured RMSE for different SNR levels is illustrated in figure 5. In agreement with the qualitative results, the RMSE represents the standard deviation of the differences between predicted and generated field map values using the three methods. In the presence of low SNR (≤ 10), SWFM and LLSf recover the field map yielding the smallest error (<1 Hz). With increasing SNR (>10), the performance of both methods is approximately similar (about 0.1 Hz). Note that beyond SNR = 20, the trend in accuracy of SWFM and LLSf is reversed (see enlarged sub-figure). The RMSE of the complex division approach was the highest for all SNRs. The method shows, however, enhancement in recovering the field map in the presence of high SNR (>20).

Figure 6 shows field map histograms over all image slices for the three methods. In comparison with the original histogram (red plot), SWFM and LLSf recover the same symmetrical field distribution about the mean ΔB of -2 Hz even in the presence of extremely low SNR. The presence of noise, which appears like peaks, however, affects the field map generation quality at different levels. CD fails completely to generate the field map in the presence of low SNR (≤ 5), which makes the histogram appear wider and the resulting field values fall out of the reference range. Similar to LLSf, the proposed approach achieves a high histogram overlap in the presence of high SNR.

4.2. *In vivo* human study

In the *in vivo* human study shown in figure 7, we can observe a phase jump at the very edge of the brain near the paranasal sinuses and cingulate region (red arrow) in phase at TE = 7.2 ms. If the phase difference map is computed without any phase unwrapping (figures 7(d) and (j)), phase aliasing and wraps may appear, and their intensity may be amplified (green arrows). As a first step, the proposed technique unwraps phase images over the temporal dimension. One can observe that residual phase wraps still exist, especially near the caudate region (yellow arrows in figures 7(e) and (k)). Conversely, wraps near the paranasal sinus were unwrapped with success. The second step consists of selecting only image slices that contain wraps and applying an additional spatial unwrapping. Selective unwrapping showed no phase errors and yielded plausible results throughout the brain (figures 7(f) and (l)).

High resolution field maps over regime I (see acquisition 2 in table 1) are generated using all mentioned algorithms. In figure 8, LLSf fails in estimating phase offsets in the presence of sharp phase aliasing and wraps



(green arrow) near the cingulate and caudate region, but otherwise yielded good results elsewhere. CD was shown to be the noisiest technique, suffering greatly from phase discontinuities near paranasal sinus and brain periphery (yellow arrows). SWFM showed no phase errors and yielded convincing results where other methods failed before.

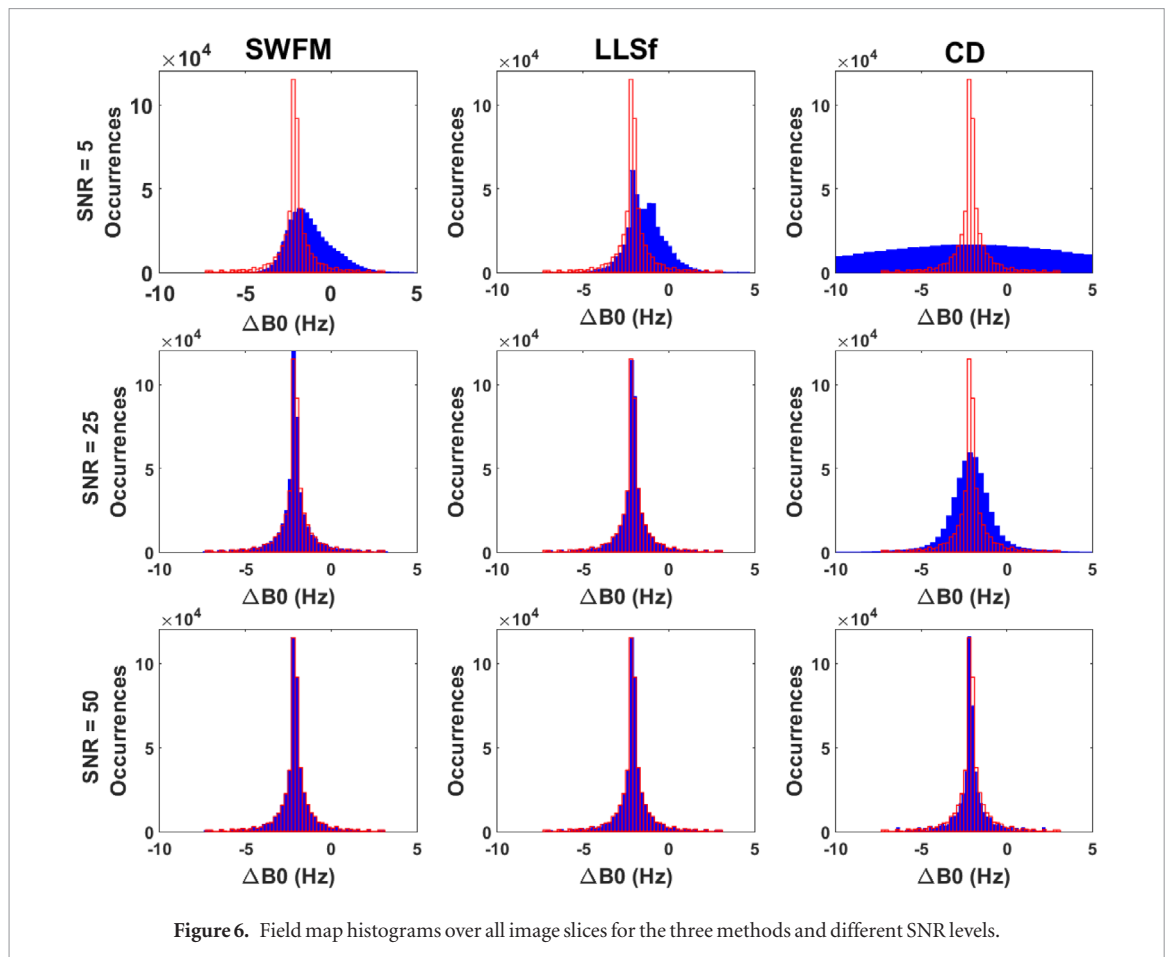


Figure 6. Field map histograms over all image slices for the three methods and different SNR levels.

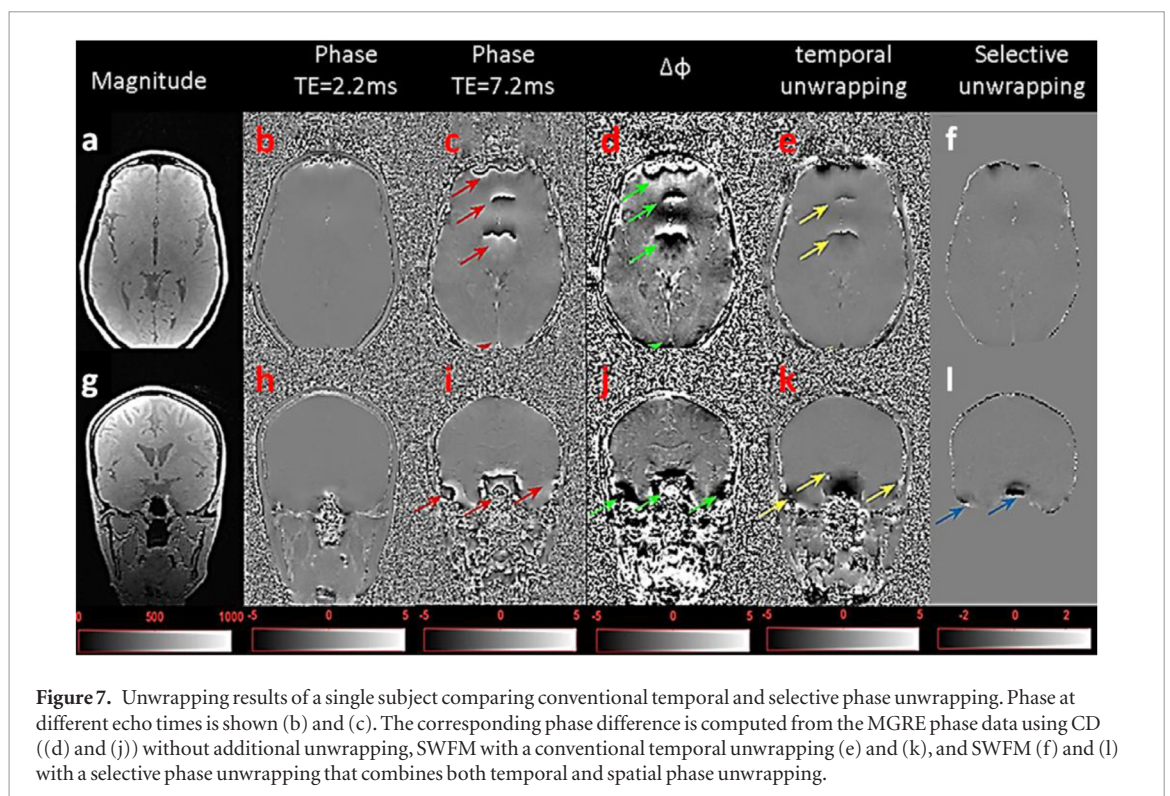


Figure 7. Unwrapping results of a single subject comparing conventional temporal and selective phase unwrapping. Phase at different echo times is shown (b) and (c). The corresponding phase difference is computed from the MGRE phase data using CD ((d) and (j)) without additional unwrapping, SWFM with a conventional temporal unwrapping (e) and (k), and SWFM (f) and (l) with a selective phase unwrapping that combines both temporal and spatial phase unwrapping.

Figure 9 shows low resolution field maps over regimes II–III (see acquisition 1 in table 1), generated using the three methods. As expected, the proposed approach shows a better performance in generating a field map with good quality. The noise is significantly reduced, and coil combination artefacts are also diminished (red arrows).

CD shows the worst performance compared to the other methods, remaining more sensitive to noise amplification, coil combination and wrapping artefacts, especially near regions with high field inhomogeneities (e.g.

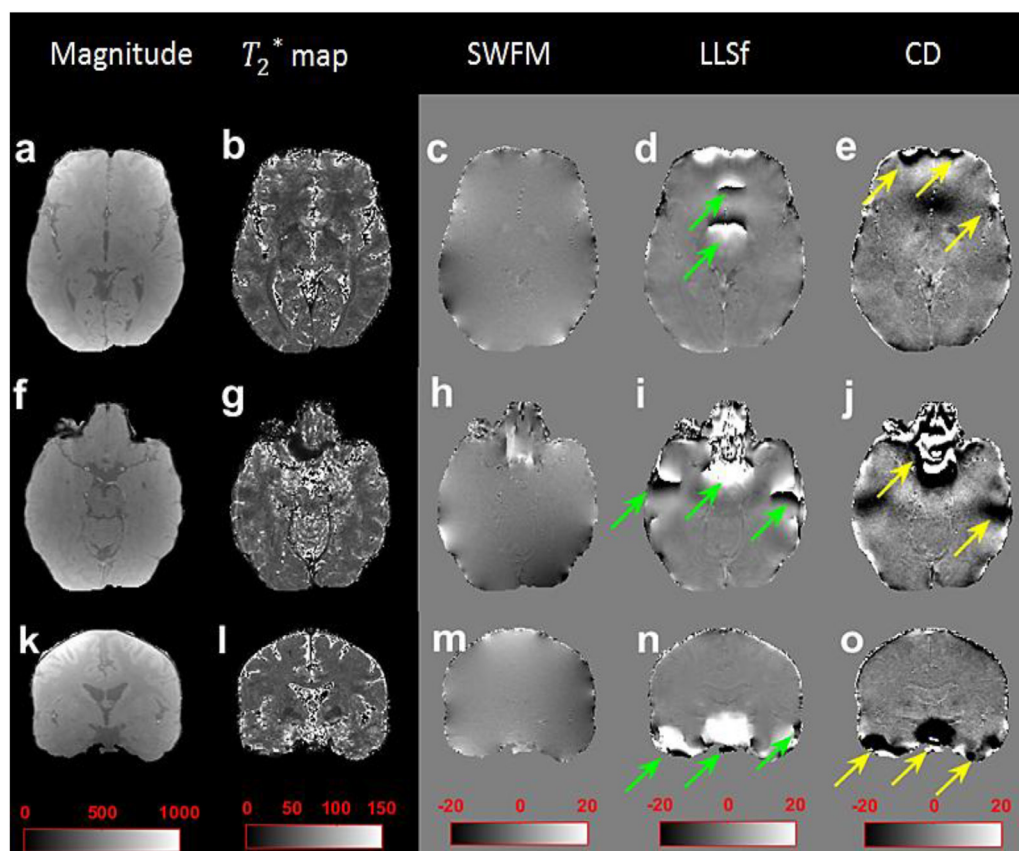


Figure 8. *In vivo* high resolution field maps over regime I results of a single subject (two axial slice levels (a)–(j) and coronal (k)–(o) slices) comparing SWFM, LLSf and CD techniques. Magnitude and T_2^* [Hz] maps are illustrated. Unwrapping errors and noise are marked with green and yellow arrows. Field map scales are in Hz.

paranasal sinuses and brain edges). SWFM and LLSf perform a high quality field mapping in a similar way in regions with a homogeneous field (center of the brain), but a little sensitivity to noise in regions with low SNR is still observed when using LLSf near lower brain edges and buccal cavity (green and red arrows in figures 9(h)–(t)). Among the evaluated methods, the proposed approach performs markedly better when the SNR is either high (center of the brain) or low (near brain edges and paranasal sinus).

5. Discussion

Simulated and *in vivo* human studies presented in the previous section highlight the main features of the proposed approach for generating the field map. Unlike previous studies, our aim was to validate the proposed approach using a gold standard reference field map. The analytical solution of the field distribution described in the Methods section was an efficient tool to simulate offset with different orientations regarding the main static field B_0 .

The presented analytical field mapping technique, which differs from numerical like LLSF, elegantly combines a complex division approach and an analytical linear regression with signal quality metrics as an optimizer and a fast selective phase unwrapping. SWFM major gain resides in the way used to compute the field map for multi-echo GRE acquisition (>3 echoes) using a fixed or variable ΔTE and also for long TE acquisitions ($TE > 40$ ms). Regardless of the phase behaviour in the presence of noise or strong field gradient that may distort the phase linearity beyond certain echo times, SWFM maps the field variation with certain constant accuracy and without any specific imposed sequence parameters.

As a consequence of the angular dependence of the external field on θ and Φ , the resulting magnetic field around a cylinder perpendicular to the magnetic field is characterized by a flower shaped appearance that increases spatial complexity. SNR dependence was also introduced to allow robust evaluation of algorithms in worst case scenarios. Furthermore, what is thought to be standard for field generation (Dahnke and Schaeffter 2005, Aksit *et al* 2007, Yablonskiy *et al* 2013) (e.g. LLSf method) for MGRE may introduce errors when linear phase evolution with time is corrupted by noise or strong macroscopic field inhomogeneities.

One should note that phase wraps complexity and signal evolution as a function of echo times are more complex in the long bipolar GRE acquisitions used in this work. ‘Unipolar’ approaches acquire all echoes using the same gradient polarity, while ‘bipolar’ approaches provide more efficient acquisitions with data collected during both positive and negative gradient lobes. Bipolar methods may be polluted by phase errors that may result from eddy currents and gradient delays that can differ for positive and negative gradient lobes. If the image voxel contains more than one tissue type, the inter-echo phase consistency may be disturbed by the phase cancellation effect, possibly leading to complex wraps, additional noise and ringing artefact appearance in the corresponding magnitude data. Recently, Fatnassi *et al* (2015) introduced a method based on ‘Odd Even’ modulation correction to address this issue. For more details, we refer the readers to Fatnassi *et al* (2015a).

The simulation results indicate that in the presence of low or high SNR, the proposed method performs field mapping with accuracy comparable to LLSf and outperforms the CD method. The technique was shown to overcome noise and spatial complexity issues by including all echoes information and weighting phase pixel values by the corresponding magnitude signal decay quality. The commonly used CD method failed to generate accurate field maps in the presence of extremely low SNR (figures 4 and 5). The presence of noise and other artefacts (e.g. coil combination, small phase wraps ...) in the phase data may be amplified, which can be explained by the fact that noise distribution may differ from one echo to another. Thus, performing complex division will accumulate noise rather than canceling it. Nevertheless, denoising data before performing complex division may result in low resolution phase images. It was also shown that CD suffers from phase discontinuities near phantom edges. At high SNR, the latter method provides an accurate field map. We believe, however, that taking into consideration echoes at long TE may add precious information about gradient severity evolution with time. Thus, CD may be highly recommended only for dual echo acquisition.

The quantitative behaviour of each method as a function of SNR using the mean of the RMSE metric (figure 5) indicated that both the proposed approach and LLSf achieve the lowest error in estimating the field map in the presence of low SNR. Under such extreme conditions, CD fails totally in recovering realistic offset values. The field mapping error occurs essentially in regions with high noise distribution and near the edges where the susceptibility effects are strong. At high SNR, all methods achieve an accurate field map.

One should note that the proposed approach was shown to outperform the LLSf method beyond a SNR of 20. As the field map computation is weighted by the signal intensity ratio ψ_j , the field estimation is more dependent on early echoes, which present higher SNRs. At large echo times, the SNR decreases and the last echoes play a minor role in estimating the field map. Reducing the impact of noisy echoes provides better results than fitting all echoes. Linear regression (LLSf) tends to estimate the phase slope using LLSf. This technique remains, however, subject to small noisy echoes even when using a good optimizer. The optimization attempts to minimize the sum of squares of errors between phase data and linear fit function. Nevertheless, the noisy echoes at large TE still have the same weight as the first ones. Consequently, the field map values after fitting may be slightly biased even for high image quality.

Unlike the complex division, in cases of extremely low SNR, SWFM and LLSf were able to attain an acceptable offset map distribution (figure 6). The large distribution yielded by CD reflects the fact that this approach remains the noisiest method evaluated. Noise tended to be located near the cylinder interfaces and around the flower-shaped appearance where the complexity of phase wraps may be higher than elsewhere. At high SNR, all methods produced a good field mapping, although SWFM and LLSf provided a considerable improvement in accuracy and the field distribution histogram was similar to the reference one (high overlap). It should be emphasized that even in the presence of high SNR, contrary to expectations, methods based on linear fitting may not deliver the most accurate results. One can observe that the presence of noise in the last echoes may influence the fit process and introduce a bias in the field map values. Therefore, using it as a gold standard for evaluating new algorithms should be performed cautiously.

The selective phase unwrapping that our method uses was shown to be valuable for unwrapping highly wrapped phase when a large ΔTE is used (regime I). As demonstrated in figure 7, the temporal technique unwraps with success phases near the paranasal sinus region and at the brain edges. It fails around the caudate and cingulate regions, however. This may be explained by the fact that spatial topography of phase wraps is of extreme complexity. Even if the temporal phase aliasing (difference between two successive voxels lies outside $[-\pi \pi]$) may be removed by adding or subtracting the proper multiple of π , the sharp spatial wraps (sharp transition between two neighbouring voxels) still exist between adjacent voxels and may never be properly unwrapped for field map regime I ($\Delta TE > 2$ ms). Fortunately, residual wraps after the temporal unwrapping appear only on a few slices. Consequently, selecting only those slices for a fast spatial unwrapping drastically decreased processing time. We should highlight that for regime II–III (moderate to small ΔTE), temporal unwrapping may be sufficient and no additional spatial unwrapping is needed.

Similar to the simulation study, the presence of noise and other artefacts (e.g. susceptibility and coil combination artefacts) lead to poor field map estimation in the *in vivo* data (figures 8 and 9). The proposed approach shows an enhancement in removing noisy regions and coil combination artefacts that are highly present in

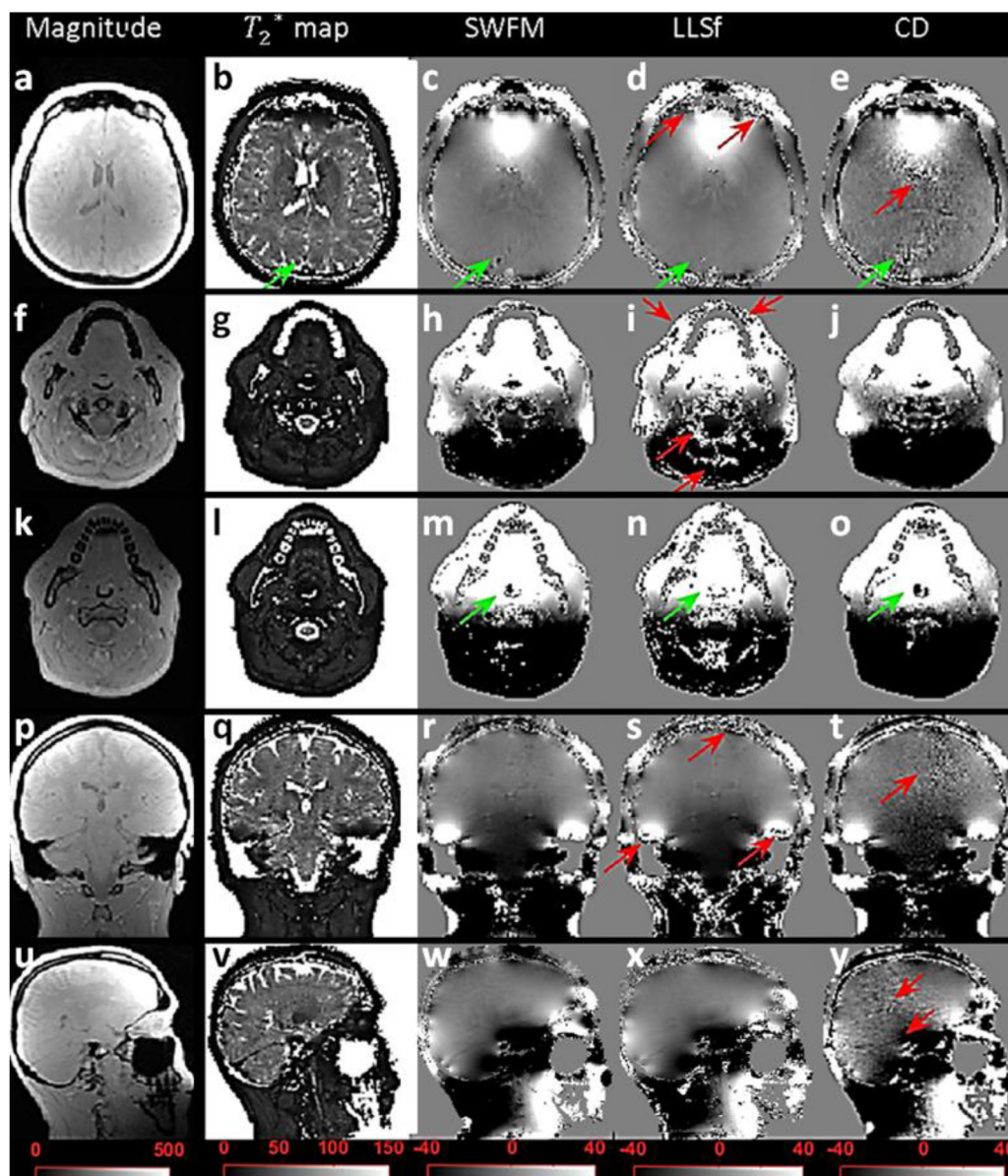


Figure 9. *In vivo* low resolution field maps over regimes II–III results of a single subject (three axial slice levels (a)–(o), coronal (p)–(t) and sagittal (u)–(y) slices) comparing SWFM, LLSf and CD techniques. Magnitude and T_2^* [Hz] maps are illustrated. Main differences between methods are marked with green and red arrows. Field map scales are in Hz.

regimes II–III (figure 9). Regions with high phase discontinuities and complex wraps (see arrows on coronal slice) are well recovered. These artefacts remain highly visible when the field map is computed using the other models, especially the CD technique. We can also notice that other algorithms have most of their errors in regions with high susceptibility artefacts (e.g. near the paranasal sinuses, brain edges and around the buccal cavity). The proposed method tends to smoothly follow the field variations in both low and high SNR regions, hence estimating the field map with good accuracy. Moreover, SWFM does not use any additional form of spatial regularization or filtering, which renders the method highly suitable for both low and high resolution field mapping.

It is recognized that coil combination remains a very challenging issue. Phase data is reconstructed from the multiple receivers using a square root of the sum of the squares algorithm, including each channel noise. However, this technique introduces some visible artefacts on phase images. Multi-coil combination is beyond the scope of this work. If no large motion is detected between acquisitions, we can assume that artefacts are introduced in the same amount during phase reconstruction for each echo. Based on this assumption, the artefact will shift the phase signal by the same amount across echo times; consequently, performing a phase difference may cancel or significantly reduce this effect. Results shown in figure 9 are in agreement with our assumption.

Short acquisitions are suitable for susceptibility weighted imaging or quantitative susceptibility mapping but may not be suitable for quantitative multiple sclerosis studies (quantitative T_2^* and MTR maps). Parametric mapping strategy for quantifying T_2^* was found to be optimal with at least eight acquired echoes (with used

TEs and Δ TEs values). Large Δ TE may create complex phase wraps when large TE introduces more noise, thus decreasing the SNR quality. Nevertheless, SWFM overcomes these issues and establishes the best possible field map for different ΔB regimes and variable Δ TEs.

Overall, the proposed algorithm was found on average to be accurate in estimating the field map in both simulation and *in vivo* studies. SWFM took less than 1 min on a standard PC to generate a field map from 40 echoes (matrix size of $136 \times 136 \times 112$), compared to more than 15 min when using the LLSf method. Hence, the use of parallel or distributed computation would allow for further reductions in calculation time. The proposed approach can therefore be implemented to generate the field map in MGRF acquisition workflow.

6. Conclusion

A large number of studies have focused on generating the field map from the phase data, which can be used to correct for macroscopic field inhomogeneities in MGRF sequences. The complexity of the problem, however, demands supplementary research and development efforts. In this work, we presented a robust analytical weighted field mapping method, where the effects of noise and other artefacts are suppressed or significantly reduced by weighting data points by the magnitude signal quality, which makes the field estimation more accurate and dependent on the early echoes that have better SNR. Even though the acquisition Δ TEs are large (regime I), field maps are accurately estimated and complex phase wraps are removed without requiring extra time. The proposed algorithm provides similar or better performance than the other methods in the presence of both low and high SNR. The new technique shows promise for improving field map generation, resulting in high robustness and reduced computation time.

Acknowledgments

This work was supported by the Swiss National Science Foundation under grant No. SNSF 320030_176052 and the Swiss Cancer Research Foundation under Grant KFS-3855-02-2016. The authors would like to thank Siemens ACIT team for sharing the *in vivo* data.

Conflict of interest

The authors declare that they have no conflict of interest.

ORCID iDs

Habib Zaidi  <https://orcid.org/0000-0001-7559-5297>

References

- Aksit P, Derbyshire J A and Prince J L 2007 Three-point method for fast and robust field mapping for EPI geometric distortion correction *IEEE Int. Symp. Biomed Imaging (ISBI)* pp 141–4
- An H and Lin W 2003 Impact of intravascular signal on quantitative measures of cerebral oxygen extraction and blood volume under normo and hypercapnic conditions using an asymmetric spin echo approach *Magn. Reson. Med.* **50** 708–16
- Bernstein MA, King KE and Zhou X J 2004 Phase difference reconstruction *Handbook of MRI, Pulse Sequences* (New York: Elsevier) pp 557–67
- Costantini M 2002 A novel phase unwrapping method based on network programming *IEEE Trans. Geosci. Remote Sens.* **36** 813–21
- Cusack R and Papadakis N 2002 New robust 3D phase unwrapping algorithms: application to magnetic field mapping and undistorting echoplanar images *NeuroImage* **16** 754–64
- Dagher J, Reese T and Bilgin A 2014 High resolution, large dynamic range field map estimation *Magn. Reson. Med.* **71** 105–17
- Dahnke H and Schaeffter T 2005 Limits of detection of spio at 3.0 T using T2 relaxometry *Magn. Reson. Med.* **53** 1202–6
- Fatnassi C, Boucenna R and Zaidi H 2015a Numerical Simpson's rule for real time and accurate T2* maps generation using 3D quantitative GRE *World Congress on Medical Physics and Biomedical Engineering* vol 51 pp 107–10
- Fatnassi C, Boucenna R and Zaidi H 2015b Unwrapping highly wrapped phase using nonlinear multi-echo phase unwrapping *World Congress on Medical Physics and Biomedical Engineering* vol 51 pp 115–8
- Fatnassi C, Boucenna R and Zaidi H 2017 Mixed model phase evolution for correction of magnetic field inhomogeneity effects in 3D quantitative gradient echo based MRI *Med. Phys.* **44** 3739–51
- Funai A K, Fessler JA, Yeo T B, Olafsson V T and Noll D C 2010 Regularized field map estimation in MRI *IEEE Trans. Med. Imaging* **27** 1484–94
- Gati J, Menon R and Ugurbil K 1997 Experimental determination of the bold field strength dependence in vessels and tissue *Magn. Reson. Med.* **38** 296–302
- Ghiglia D C and Romero LA 1994 Robust two-dimensional weighted and unweighted phase unwrapping that uses fast transforms and iterative methods *J. Opt. Soc. Am.* **11** 107–17
- Grandin C 2003 Assessment of brain perfusion with MRI: methodology and application to acute stroke *Neuroradiology* **45** 755–66

- Haacke E M, Cheng N Y, House M J, Liu Q, Neelavalli J, Ogg R J, Khan A, Ayaz M, Kirsch W and Obenaus A 2005 Imaging iron stores in the brain using magnetic resonance imaging *Magn. Reson. Imaging* **23** 1–25
- Hernando D, Vigen K, Shimakawa A and Reeder S 2010 R2* mapping in the presence of macroscopic B₀ field variations *Magn. Reson. Med.* **68** 830–40
- Jezzard P and Balaban R S 1995 Correction for geometric distortion in echo planar images from B₀ field variations *Magn. Reson. Med.* **34** 65–73
- Reber P J, Wong E C, Buxton R B and Frank L R 1998 Correction of off resonance-related distortion in EPI using EPI-based field maps *Magn. Reson. Med.* **39** 328–30
- Robinson S, Schödl H and Trattnig S 2014 A method for unwrapping highly wrapped multi-echo phase images at very high field: UMPIRE *Magn. Reson. Med.* **72** 80–92
- Seara M F and Wehrli F 2000 Post processing technique to correct for background gradients in image-based R2* measurements *Magn. Reson. Med.* **44** 358–66
- Windischberger C, Robinson S, Rauscher A, Barth M and Moser E 2004 Robust field map generation using a triple-echo acquisition *J. Magn. Reson. Imaging* **20** 730–4
- Wirestam R, Thilmann O, Knutsson L, Burtscher I B, Larsson E and Stahlberg F 2010 Comparison of quantitative dynamic susceptibility contrast MRI perfusion estimates obtained using different contrast agent administration schemes at 3T *Eur. J. Radiol.* **75** 86–91
- Yablonskiy D A 1998 Quantitation of intrinsic magnetic susceptibility related effects in a tissue matrix: phantom study *Magn. Reson. Med.* **39** 417–42
- Yablonskiy D A, Alexander L, Luo S J and Wang X 2013 Voxel spread function method for correction of magnetic field inhomogeneity effects in quantitative gradient echo based MRI *Magn. Reson. Med.* **70** 1283–92
- Yang X, Sammet S, Schmalbrock P and Knopp M 2010 Post-processing correction for distortions in T2* decay caused by quadratic cross slice B₀ inhomogeneity *Magn. Reson. Med.* **63** 1258–68
- Zwaag W V, Francis S, Head K, Peters A, Gowland P, Morris P and Bowtell R 2009 fMRI at 1.5, 3 and 7 T: characterizing bold signal changes *NeuroImage* **47** 1425–34